arXiv:0810.0007v1 [astro-ph] 30 Sep 2008

Column Densities Towards Three Bursting Low-Mass X-ray Binaries from High Resolution X-ray Spectroscopy

Patricia Wroblewski, Tolga Güver, and Feryal Özel

University of Arizona, Departments of Astronomy and Physics, 933 N. Cherry Ave., Tucson, AZ 85721

ABSTRACT

We measured the galactic hydrogen column densities to the neutron-star binaries GX 17+2, 4U 1705−44, and 4U 1728−34 by modeling the Mg and Si absorption edges found in high-resolution X-ray spectra obtained by the Chandra X-ray Observatory. We found for GX 17+2, $N_{\rm H} = (2.38 \pm 0.12) \times 10^{22}$ cm^{-2}, for 4U 1705−44, $N_{\rm H} = (2.44 \pm 0.09) \times 10^{22}$ cm^{-2}, and for 4U 1728−34, $N_{\rm H} = (2.49 \pm 0.14) \times 10^{22}$ cm^{-2}. These values are in reasonable agreement with the hydrogen column densities inferred earlier from modeling of the continuum spectra of the sources. Our results can be used to constrain the uncertainties of model parameters of the X-ray spectra of these sources that are correlated to the uncertainties of the hydrogen column density. In the case of continuum spectra obtained during thermonuclear X-ray bursts, they will significantly reduce the uncertainties in the spectroscopically measured masses and radii of the neutron stars.

Subject headings: X-rays: ISM, X-rays: binaries, stars: neutron, stars: individual (GX 17+2, 4U 1705−44, 4U 1728−34)

1. Introduction

Low-mass X-ray binaries (LMXBs) that show thermonuclear bursts are ideal targets for measuring the masses and radii of neutron stars. During these short-lived flashes, the flux from the stellar surface dominates the persistent luminosity by up to two orders of magnitude and can often reach the local Eddington limit. Owing to their low magnetic fields, inhomogeneities in the surface emission are neither observed (e.g., Galloway et al. 2003), nor theoretically expected, during the peak of the bursts. Modeling time resolved X-ray spectra during these bursts can, thus, lead to an accurate measurement of either the gravitational redshift, or, if the distance to the source is also known, to a measurement of the mass and the radius of neutron star (van Paradijs 1978; Damen et al. 1990; Lewin, van Paradijs, & Taam 1993; Özel 2006; Özel, Güver, & Psaltis 2008).

Accurate measurements of column densities towards the bursting LMXBs are important for two reasons. First, X-ray spectra are attenuated by the interstellar medium (ISM) due to photoelectric absorption and scattering by dust grains. When X-ray spectra, particularly in the soft X-ray band

(0.1-10 keV), are used to measure the effective temperature of the neutron star, $T_{\rm eff}$, and its radius R, this extinction affects the modeling of continuum spectra, the inferred temperature, and, thus, the measured stellar radius. Because of the $R \sim T_{\rm eff}^{-2}$ scaling of the measured radius, uncertainties in the column density can give rise to large errors in radius. The spectral parameters are indeed very sensitive to the assumed or allowed values of the hydrogen column density. We show in Figure 1 an example of the correlated uncertainties between the temperature and the column density for the X-ray spectrum of 4U 1728−34 taken with the Rossi X-ray Timing Explorer Proportional Counter Array during a thermonuclear burst. Such correlations alone can lead to $\gtrsim 15\%$ uncertainties in stellar radii.

Second, measuring the column of interstellar extinction towards an X-ray source facilitates the use of a novel distance determination technique based on red clump stars along the line of sight to the source. The red clump stars are excellent infrared standard candles (Paczynski & Stanek 1998; Lopez-Corredoira et al. 2002) that can be used to measure the run of reddening with distance. This method establishes a distance ladder in the galaxy, which can then be compared to the extinction of X-ray sources that is determined by their high resolution spectra to determine their distances.

An independent measurement of the X-ray column density through a grating observation, where the photoelectric absorption edges of each element within the observational window can be determined, is valuable for correctly computing the spectral parameters of these binary systems. This is a method that has been previously applied to LMXBs by Juett, Schulz, & Chakrabarty (2004) and Juett et al. (2006), who measured the O, Ne, and Fe edges in their spectra obtained with the Chandra High Energy Transmission Grating (HETG) and XMM-Newton. It has also been employed in the case of Anomalous X-ray pulsars by Durant & van Kerkwijk (2006).

In this paper, we analyze Chandra HETG spectra taken during numerous observations of GX 17+2, 4U 1705−44, and 4U 1728−34. These binaries do not have previously measured hydrogen column densities from absorption edges in high-resolution X-ray grating spectra. We report the equivalent column densities for each of the measurable edges, investigate any possible systematic uncertainties, and compare our findings with column densities obtained previously from continuum spectra for these sources.

All three sources have shown frequent thermonuclear (Type-I) X-ray bursts, with a total number as high as 106 in the case of 4U 1728−34 (Galloway et al. 2008). A large number of these bursts (e.g., 69 for the last source) also showed characteristic photospheric radius expansion properties, indicating that the local Eddington limit has been reached. Thus, they are ultimately good candidates for the measurement of the neutron star mass and radius. Given their locations in the galactic plane, extinction towards these sources can also be used to study the properties of the ISM in the Galaxy.

2. Observations and Data Reduction

The low-mass X-ray binaries GX 17+2, 4U 1705−44, and 4U 1728−34 were observed multiple times with the High Energy Transmission Grating Spectrometer (HETG) onboard the Chandra X-ray Observatory. Our study includes a total of nine archival observations of these three sources. The HETG consists of the Medium Energy Gratings (MEG), with a $2.5 - 31$ Å wavelength range and a resolution of $\delta\lambda = 0.023$ Å (for the first-order spectra), and the High Energy Gratings (HEG),with a $1.2 - 15$ Å range and a resolution of $\delta\lambda = 0.012$ Å.

The three observations of GX 17+2, with 30.18 ks, 23.68 ks, and 24.08 ks durations, were all taken in the continuous clocking (CC) mode between 2004 and 2006. Both observations of 4U 1705−44 were taken in the timed exposure (TE) mode, for a total exposure of 25.13 ks in 2001 and 27.25 ks in 2005. 4U 1728−34 has been observed four times, with exposure times of 10 ks (in 2002), 151.84 ks (in 2006), 49.49 ks (in 2006), and 39.71 (in 2006). The first observation in 2002 was in TE mode, while all the subsequent observations have been performed in the CC mode. We list in Table 1 the observations included in our study, together with the average count rate in each observation.

The spectral data were reduced following standard CIAO threads[1] using the CIAO version 4.0.1 and CALDB 3.4.3. Different threads were used for continuous clock and timed event modes due to the variations in the calibration. For observations performed in a timed exposure mode, the high fluxes of the sources can cause a pile-up in the zeroth order (undispersed) images. This can give rise to problems in determining the exact zero-order position of the source, which can ultimately shift the wavelength scale of the grating spectrum. For this reason, we have made use of the findzo.sl[2] files, which use the MEG arms and the frame-shift streak to find the best fit zero-order position. Additionally, for both types of observations, we excluded any observed Type-I bursts, which have different continuum spectra and may also have local heavy-element features.

Detector response files (ARFs) were created for the +1 and −1 MEG and HEG spectra for both the TE mode and the CC mode observations. Note that the ARFs include the correction for any time-dependent change due to a contaminant on ACIS. For the TE mode observations, the +1 and −1 orders were combined together for both the MEG and the HEG spectra. However, two concerns rendered the MEG +1 order of the CC mode observations unusable. First, there is an instrumental feature in the O edge on the MEG +1 side (Juett, A., Private Communication). Second, all the observations we studied were carried out with either a $0.33'$ or $0.1667'$ offset, which caused the wavelength of the Mg edge to fall in or near chip gaps. In the CC mode, this resulted in a complete reduction of the effective area at that wavelength, while in the TE mode, there were sufficient counts that were included in the analysis. Figure 2 shows a sample observation from 4U 1728−34, where the effective areas of each grating and order can be seen. Finally, all MEG data were binned by a factor of 4 and the HEG data were binned by a factor of 8 to increase the statistics while achieving the same energy resolution on both gratings.

3. Spectral Analysis

We originally sought to measure the edges of neutral Mg, Si, Ne, O, and Fe in the HETG spectra of GX 17+2, 4U 1705−44, and 4U 1728−34. However, the source count rates were typically very low at long wavelengths, leading to negligible flux around the O and Fe edges for all the sources. Near the Ne edge, at a wavelength of 14.31 Å (Juett et al. 2006), the continuum was detectable but there were not enough counts for any of the sources to yield statistically significant results. We thus considered only the Mg and Si edges in our analyses.

We focused on small wavelength regions around the Mg and Si edges and assumed that the continuum spectrum of each source could be fit with a power-law in each of these regions, $F_\lambda^c \propto (\lambda/\lambda_{\rm edge})^\alpha$, with a break at the absorption edge of interest. We used fixed edge wavelengths: $\lambda_{\rm Mg} = 9.5$ Å for the location of the Mg edge and $\lambda_{\rm Si} = 6.72$ Å (Ueda et al. 2005) for the Si edge. We modeled each edge by fitting a function of the form

$$F_\lambda = \begin{cases} F_\lambda^c & {\rm for} \lambda > \lambda_{\rm edge} \\ F_\lambda^c \exp\left[-A\left(\frac{\lambda}{\lambda_{\rm edge}}\right)^3\right] & {\rm for} \lambda \leq \lambda_{\rm edge} \end{cases} \quad (1)$$

We adjusted the specific wavelength range that we used in the fits for each source because of small variations in the intrinsic continuum spectra of the sources. However, between the multiple observations of a given a source, we froze the range that we analyzed. Specifically, for GX 17+2, we used $5.8-7.2$ Å for Si and $8.6-10.5$ Å for Mg. For 4U 1705−44, we chose a range of $5.7-7.5$ Å for Si and 8.5−10.3 Å for Mg. Finally, for 4U 1728−34, we used $5.9-7.3$ Å for Si and $8.5-10.3$ Å for Mg. Sample spectra for all three sources in these wavelength ranges are shown in Figures 3 and 4.

We fit the MEG and HEG data both separately and simultaneously to detect any possible systematic differences. For the data taken in the TE mode, the slopes obtained by fitting power-law functions to the continuum of both gratings were in good agreement with each other. Note that the pile-up fraction in one of the observations of 4U 1705−44 (Obsid: 1923) was nearly 15% around the Si edge in the MEG spectrum and this result was excluded from the final analysis. In the CC mode observations, however, there were more than 3σ differences in the power-law indices obtained for the HEG and MEG data. This is thought to be due to calibration uncertainties in this mode. Because of this, only MEG data were used for all of the fits (of the CC mode data) due to the larger photon collecting area of this grating compared to the HEG in the wavelength region of interest ($5.5-15.5$ Å).

In addition to a power-law continuum and the function modeling the edges, we allowed for a number of emission and absorption line features that appear in each spectral region and whose positions are fixed. For consistency, we included the same number of absorption and emission lines in the spectral fits of each observation of each source, regardless of the apparent presence or absence of a feature in that spectrum, as was done by Juett et al. (2006). When the features were

not detectable or were not well-constrained in a given observation, we report a zero flux for the lines. A negative amplitude corresponds to an absorption feature.

Around the Si absorption edge, we fixed the wavelengths of the five most prominent features in the wavelength range for each source using Chandra's atomic lines database ATOMDB[3]. The most prominent features in this region are the two Si XIV and three Si XIII atomic lines. In Figure 3, we show three sample spectra from each source around the Si edge, along with the fitted power-law continuum, the edge, and the line features. Table 2 shows the calculated fluxes of the emission lines for each observation.

Similarly, in the wavelength range around the Mg edge, we included Mg XI, Fe XXI, and Ne X emission features, which are the strongest. The Mg XI features at 9.16 Å, 9.22 Å, and 9.31 Å are part of a He-like triplet formed by the resonance, intercombination, and forbidden transitions (Porquet et al. 2001). We show in Figure 4 the results of our fits to the grating spectra obtained from one of the observations of each source. We report the corresponding line fluxes in Table 3 and report our findings for the Si and Mg edges in the next section.

4. Results and Discussion

We used the Chandra grating observations of GX 17+2, 4U 1705−44, and 4U 1728−34 to measure absorption coefficients for the Mg and Si edges. In Tables 2 and 3, we also report the fluxes of spectral lines that were measured in each observation around the Si and Mg edges, respectively. We then used the absorption coefficients along with the cross-sections from Gould & Jung (1991) to find the column densities for each element. We converted the Mg and Si column densities to hydrogen column densities, $N_{\rm H}$, using the ISM abundances given by Wilms, Allen, & McCray (2000). We report all of the column densities in Table 4. We then averaged the results obtained with each absorption edge over the observations, which makes it possible to discriminate any possible systematic differences between the column densities obtained from the different edges.

For GX 17+2, the $N_{\rm H}$ values derived from the Mg edge ranged from $(2.01 - 2.77) \times 10^{22}$ cm^{-2}, while the values derived from the Si edge ranged from $(1.03 - 2.69) \times 10^{22}$ cm^{-2} for the three observations. Averaging over the column densities derived from the Mg edge yields $(2.38 \pm 0.12) \times 10^{22}$ cm^{-2}, while over those derived from the Si edge results in $(1.78 \pm 0.09) \times 10^{22}$ cm^{-2}. We note that the lower $N_{\rm H}$ value derived from the Si edge can be attributed to the small edge measured in one single observation and that the remaining five measurements are consistent with each other to within 2σ.

[1]http://asc.harvard.edu/ciao/threads/

[2]http://space.mit.edu/cxc/analysis/findzo/Data/findzo.sl

[3]http://cxc.harvard.edu/atomdb/WebGUIDE/

4U 1705−44 showed a somewhat smaller scatter with equivalent $N_{\rm H}$ ranging from $(2.08 - 2.59) \times 10^{22}{\rm cm}^{-2}$ from the Mg edge measurements and $(2.95 - 4.12) \times 10^{22}{\rm cm}^{-2}$ from the Si edge measurements. Averaging over the column densities derived from the Mg edge yields $(2.44 \pm 0.09) \times 10^{22}$ cm^{-2}, and $(3.64 \pm 0.12) \times 10^{22}$ cm^{-2} from the Si edge. Because the difference between these two measurements are larger than that expected from statistical uncertainties, we treat it as a systematic difference, potentially caused by calibration errors or by anomalous abundances.

Finally, 4U 1728−34 had equivalent hydrogen column densities in the range $(2.39 - 8.23) \times 10^{22}$ cm^{-2} in individual edge measurements. However, the highest of these values, corresponding to the Silicon edge in observation 2748 (N[Si]$_{\rm H} = (8.23 \pm 0.29) \times 10^{22}$ cm^{-2}), arises from a previously reported Si overabundance that is thought to be caused from calibration problems in that specific observation (D'Aí et al. 2006). As a result, we excluded this measurement when calculating the average hydrogen column density for this source. We again calculated separate average values for each edge: we obtained $N_{\rm H} = (2.49 \pm 0.14) \times 10^{22}$ cm^{-2} from the Mg edge and $(4.27 \pm 0.14) \times 10^{22}$ cm^{-2} from the Si edge.

We detect a systematic difference between the $N_{\rm H}$ values obtained from Mg and Si edges in all of the observations. These could naturally be attributed to non-standard ISM abundances or to anomalous intrinsic abundances of the sources. However, we also observed that the scatter between the absorption coefficients at the Si edge is also much larger between the different observations of each source. Noting that the response of the detector suffers from a very large discontinuity at the Si edge but is smooth across the Mg edge, we investigated whether these differences could be due to small inaccuracies in the detector response across the Si edge. In particular, we explored whether there is any dependence of this systematic variation on the source count rate during the observations. We found that when the count rates of the sources are on average higher (~ 30 cts s^{-1}), the N$_{\rm H}$ values found using the two edges become consistent with each other to within 2σ, and that the discrepancy between the two values increases as the source count rate decreases. This is especially evident in the two spectra of 4U 1705−44, where one of the two spectra of this source was obtained when the source count rate was 38.6 cts s^{-1} while the second observation was performed during a smaller count rate epoch (12.6 cts s^{-1}). We note that between these observations the N$_{\rm H}$ value found from the Mg edge does not change significantly, while the value found from the Si edge increases and the difference between the two measurement becomes as much as 10σ.

Given that the intrinsic metal abundance of the X-ray binary or the metal abundances in the ISM is unlikely to change significantly for the same source within 4 years, we conclude that the difference might arise because of the presence of the significant intrumental Si edge, where small uncalibrated residuals of this structure affect our edge measurements. Because of this, we will use $N_{\rm H}$ measurements from the Mg edges as the preferred values.

We have also compared our measurements of hydrogen column densities towards these three sources determined from the overall suppression of low-resolution continuum spectra.

Previous estimates of the column density towards GX 17+2 were made from modeling the

continuum spectra obtained with ROSAT observations. Predehl & Schmitt (1995) found $N_{\rm H}$ values to the source in the range $(1.79-2.34)\times10^{22}$ cm^{-2}, assuming a blackbody, thermal bremsstrahlung or a power-law model for the continuum. These values span the range obtained from the Mg and Si edge measurements and are thus in agreement with our results.

Two estimates of the column density towards 4U 1705−44 exist based on observations with different satellites and using different continuum models. Predehl & Schmitt (1995) reported a range of hydrogen column densities towards towards the source using ROSAT observations. Continuum models included a blackbody, thermal bremsstrahlung or a power-law, as in the case of GX 17+2, and resulted in a range $N_{\rm H} = (1.23-1.63)\times10^{22}$ cm^{-2}. Barret & Olive (2002), on the other hand, reported a column density $N_{\rm H} = 2.4\times10^{22}$ cm^{-2} by fitting a Comptonized blackbody model to the RXTE Proportional Counter Array data. The former values are lower than the model-independent column densities we find here, while the latter value is consistent within 1σ with our results when only the Mg column is taken into account.

Observations of 4U 1728−34 by ROSAT, BeppoSax, and Chandra observatories have also yielded a range of estimates for the hydrogen column density towards this source when the data were fit with different continuum models. Schulz (1999) analyzed the ROSAT data using power-law and blackbody continuum models, which yielded hydrogen column densities $N_{\rm H} = (3.44\pm0.3)\times10^{22}$ cm^{-2} and $N_{\rm H} = (2.89\pm0.22)\times10^{22}$ cm^{-2}, respectively. BeppoSAX data were fit with a Comptonized blackbody model to give $N_{\rm H} = (2.73\pm0.05)\times10^{22}$ cm^{-2} (Piraino, Santangelo, & Kaaret 2000). Finally, the spectrum obtained with Chandra HETG was modeled with a Comptonized blackbody to give $2.61^{+.06}_{-.07}\times10^{22}$ cm^{-2} (D'Aí et al. 2006). Note that while 4U 1728−34 has also been observed with the RXTE Proportional Counter Array and Integral, the hydrogen column density was not well constrained from these observations. All but the ROSAT measurements are consistent with the column density of $N_{\rm H} = (2.49\pm0.14)\times10^{22}$ cm^{-2} measured from the Mg edge.

We thank Adrienne Juett for numerous helpful discussions and suggestions on the analysis of the grating spectra as well as her comments on the manuscript. We also thank Michael Nowak for his help with Chandra HETG. This work was supported by NSF grant AST 07-08640.

REFERENCES

Barret, D., & Olive, J.-F. 2002, ApJ, 576, 391

D'Aí, A., et al. 2006, A&A, 448, 817

Damen, E., Magnier, E., Lewin, W. H. G., Tan, J., Penninx, W., & van Paradijs, J. 1990, A&A, 237, 103

Durant, M., & van Kerkwijk, M. H. 2006, ApJ, 650, 1082

Galloway, D. K., Psaltis, D., Chakrabarty, D., & Muno, M. P. 2003, ApJ, 590, 999

Galloway, D. K., Muno, M. P., Hartman, J. M., Psaltis, D., & Chakrabarty, D. 2008, ApJS, in press (arXiv:astro-ph/0608259)

Gould, R. J., & Jung, Y.-D. 1991, ApJ, 373, 271

Juett, A. M., Schulz, N. S., & Chakrabarty, D. 2004, ApJ, 612, 308

Juett, A. M., Schulz, N. S., Chakrabarty, D., & Gorczyca, T. W. 2006, ApJ, 648, 1066

Lattimer, J. M., & Prakash, M. 2001, ApJ, 550, 426

Lattimer, J. M., & Prakash, M. 2007, Phys. Rep., 442, 109

Lee, J.-W., Carney, B. W., Fullton, L. K., & Stetson, P. B. 2001, AJ, 122, 3136

Lewin, W. H. G., van Paradijs, J., & Taam, R. E. 1993, Space Science Reviews, 62, 223

López-Corredoira, M., Cabrera-Lavers, A., Garzón, F., & Hammersley, P. L. 2002, A&A, 394, 883

Özel, F. 2006, Nature, 441, 1115

Özel, F., Güver, T., & Psaltis, D., ApJ, submitted

Paczynski, B., & Stanek, K. Z. 1998, ApJ, 494, L219

Piraino, S., Santangelo, A., & Kaaret, P. 2000, A&A, 360, L35

Predehl, P., & Schmitt, J. H. M. M. 1995, A&A, 293, 889

Porquet, D., Mewe, R., Dubau, J., Raassen, A. J. J., & Kaastra, J. S. 2001, A&A, 376, 1113

Schulz, N. S. 1999, ApJ, 511, 304

Ueda, Y., Mitsuda, K., Murakami, H., & Matsushita, K. 2005, ApJ, 620, 274

van Paradijs, J. 1978, Nature, 274, 650

Wilms, J., Allen, A., & McCray, R. 2000, ApJ, 542, 914

This preprint was prepared with the AAS LaTeX macros v5.2.

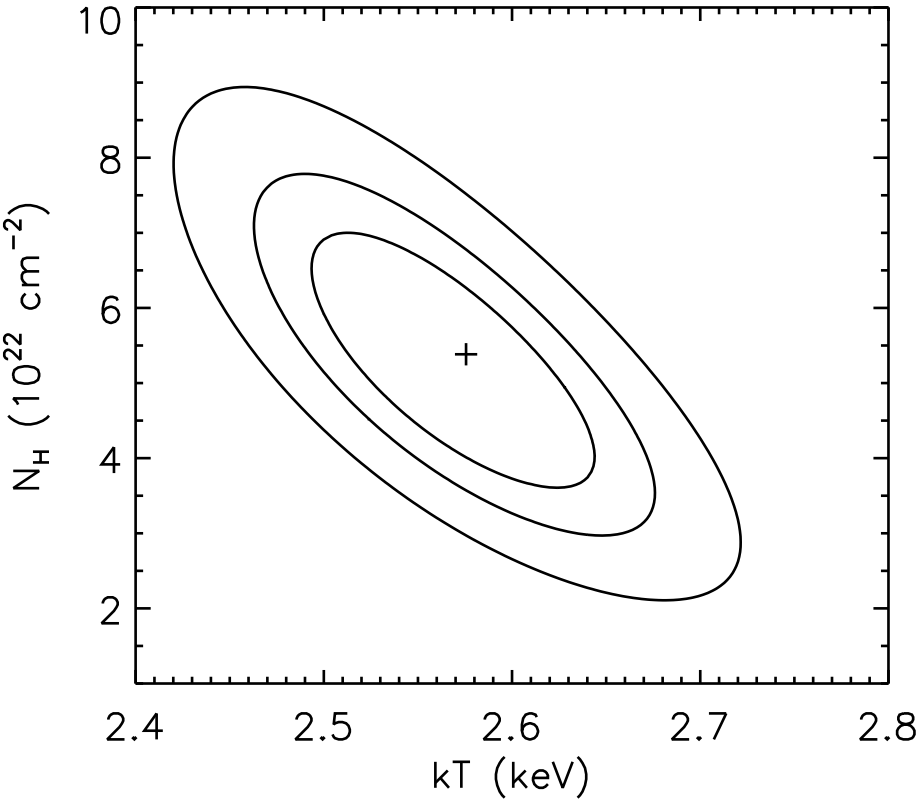

Fig. 1.— The correlation between column density and temperature is shown for 4U 1728−34 as found for one of the photospheric radius expansion bursts from an RXTE observation. The three contours show the 1σ, 2σ, and 3σ confidence levels.

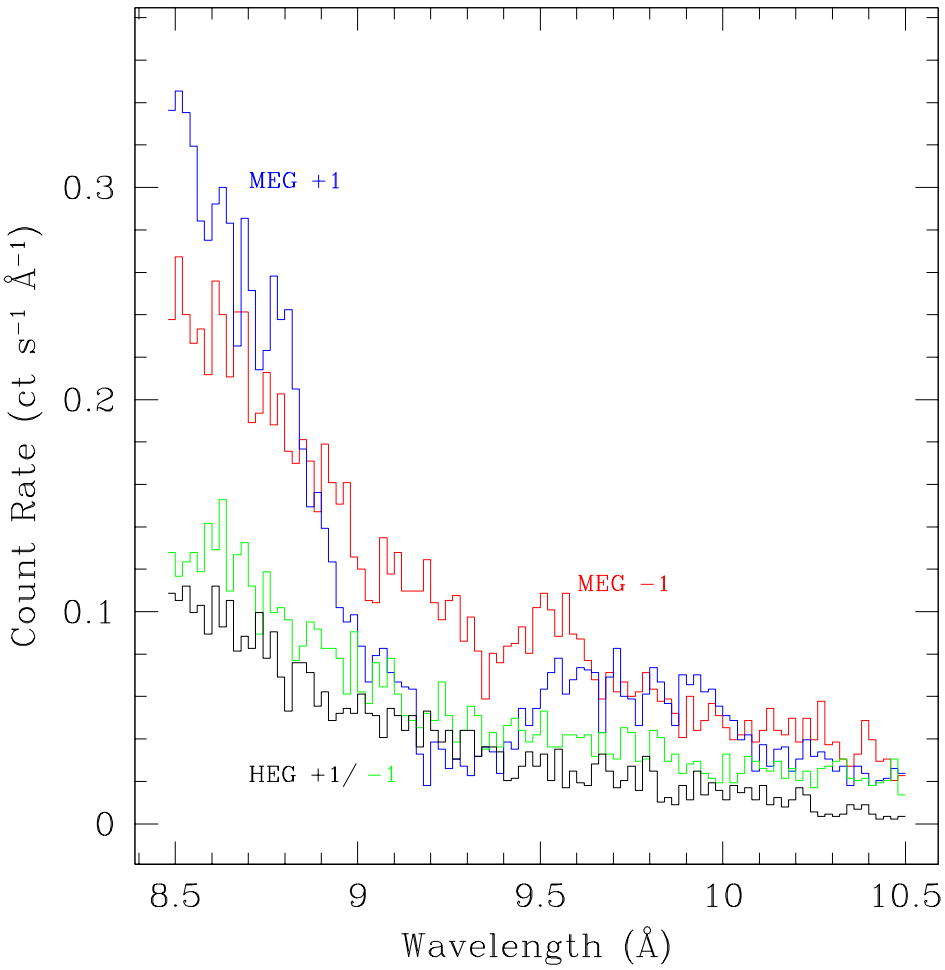

Fig. 2.— A sample spectrum of 4U 1728−34 that shows the +1 and −1 orders of both MEG and HEG gratings. In addition to intrinsic differences between the effective areas of the HEG and the MEG gratings, there is also a chip gap at the MEG +1 order aroung 9.5 $\AA$ which causes a significant reduction in the counts in this region.

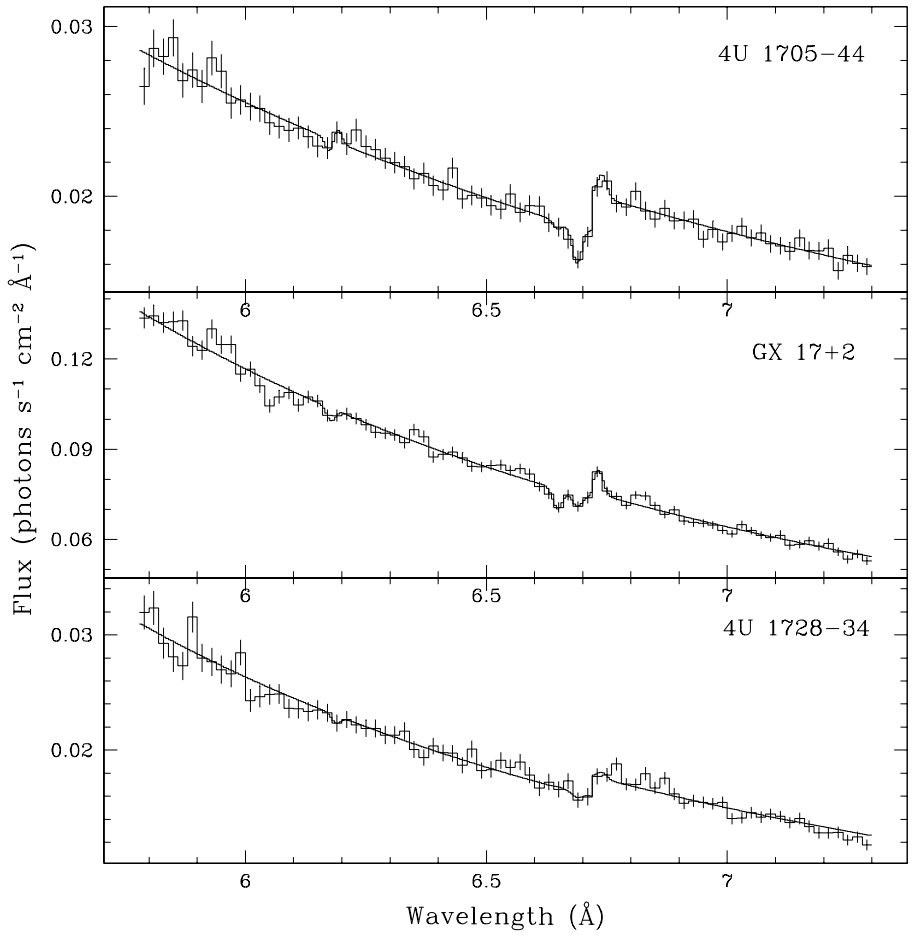

Fig. 3.— The fitted spectra for the Silicon edge. For 4U 1705−44, GX 17+2, and 4U 1728−34, obsids 5500, 4564, and 6568, are shown, respectively. Details of these fits can be seen in Table 2.

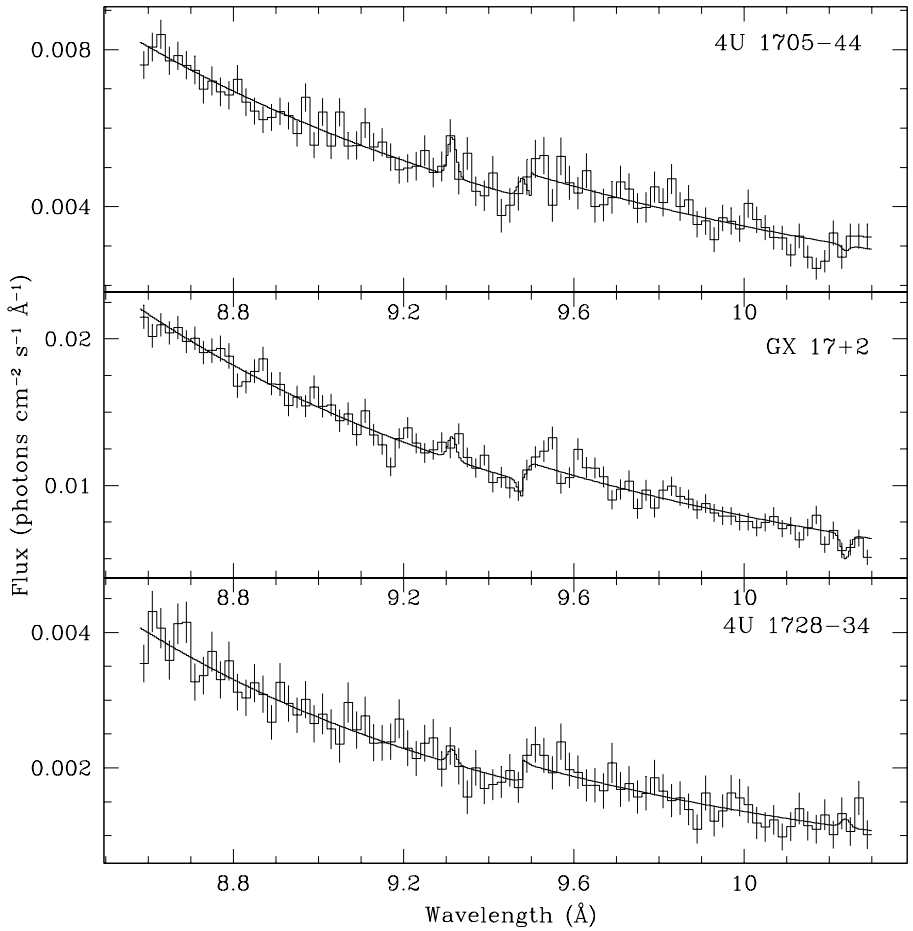

Fig. 4.— The fitted spectra for the Magnesium edge. For 4U 1705−44, GX 17+2, and 4U 1728−34, obsids 5500, 4564, and 6568, are shown, respectively. Details of these fits can be seen in Table 3.

Table 1. List of Chandra Observations by Source Used in this Study

Source	Obsid	Mode	Date	Exp. Time (ks)	Average Count Rate (ct s^{-1})
GX 17+2	4564	CC	2004 July 11	30.18	30.43
	6629	CC	2006 May 10	23.68	31.52
	6630	CC	2006 Aug 19	24.08	29.82
4U 1705−44	5500	TE	2001 July 01	25.13	12.62
	1923	TE	2005 Oct 26	27.25	38.60
4U 1728−34	2748	TE	2002 Mar 04	10.00	7.29
	6568	CC	2006 July 17	49.49	6.53
	6567	CC	2006 July 18	151.84	7.84
	7371	CC	2006 July 22	39.71	4.53

Table 2. Fluxes of Spectral Lines around the Si Edge[1]

		Flux (10^{-5} photons cm^{-1} sec^{-1} $Å^{-1}$)				
Source	Obsid	Si XIV^{2}_{a} 6.1804 Å	Si XIV_{b} 6.1858 Å	Si $XIII_{c}$ 6.6479 Å	Si $XIII_{d}$ 6.6882 Å	Si $XIII_{e}$ 6.7403 Å
GX 17+2	4564	-16.0±5.99[1]	−−	-17.3±4.8	-10.1±4.8	15.8±4.6
	6629	−−	−−	−−	-13.1±9.0	26.1±8.5
	6630	-11.7±6.85	−−	-11.7±5.8	−−	9.64±5.38
4U 1705−44	1923	−−	−−	−−	-11.03±5.46	−−
	5500	-3.43±1.76	3.93±1.69	−−	-5.59±1.46	5.42±1.44
4U 1728−34	2748	−−	1.66±1.43	2.07±1.20	3.34±1.16	−−
	6567	2.06±1.99	2.80±1.89	−−	-2.13±1.66	7.36±1.60
	6568	−−	−−	−−	−−	−−
	7371	-5.07±2.12	4.69±2.04	-4.81±1.8	−−	3.87±1.76

[1]Errors correspond to 1σ statistical uncertainties.

[2]Transitions from $^{a}4 \rightarrow 1$ $^{b}3 \rightarrow 1$ $^{c}7 \rightarrow 1$ $^{d}5 \rightarrow 1$ $^{e}2 \rightarrow 1$

Table 3. Fluxes of Spectral Lines around the Mg Edge[1]

		Flux (10^{-5} photons cm^{-1} sec^{-1} Å^{-1})				
Source	Obsid	Mg XI$_a^2$ 9.1687 Å	Mg XI$_b$ 9.2267 Å	Mg XI$_c$ 9.3143 Å	Fe XXI 9.4797 Å	Ne X 10.2385 Å
GX 17+2	4564	−−	−−	3.95±2.17	2.95±2.17	-4.37±1.58
	6629	−−	−−	−−	−−	−−
	6630	−−	−−	−−	−−	-4.98±1.91
4U 1705−44	1923	−−	−−	−−	−−	−−
	5500	−−	2.72±1.11	1.52±1.22	−−	−−
4U 1728−34	2748	−−	−−	−−	−−	−−
	6567	1.51±0.71	1.69±0.71	−−	-0.93±0.57	−−
	6568	−−	−−	−−	−−	−−
	7371	2.90±0.94	1.54±0.84	−−	−−	-0.61±0.56

[1]Errors correspond to 1σ statistical uncertainties.

[2]Transitions from $^a7 \rightarrow 1$ $^b6 \rightarrow 1$ $^c2 \rightarrow 1$

Table 4. Column Densities from Mg and Si Edges[1]

Source	Obsid	N_{Mg} 10^{17} cm^{-2}	N[Mg]$_H$ 10^{22} cm^{-2}	N_{Si} 10^{17} cm^{-2}	N[Si]$_H$ 10^{22} cm^{-2}	$\langle N_H \rangle$ 10^{22} cm^{-2}
GX 17+2	4564	5.06±0.41	2.01±0.16	1.92±0.26	1.03±0.14	
	6629	6.95±1.08	2.77±0.43	5.01±0.44	2.69±0.23	
	6630	6.96±0.44	2.77±0.18	4.33±0.29	2.32±0.16	2.38± 0.12[2]
4U 1705−44	1923	6.50±0.26	2.59±0.10	5.49±0.36	2.95±0.19	
	5500	5.23±0.41	2.08±0.16	7.66±0.30	4.12±0.16	2.44± 0.09
4U 1728−34	2748	6.38±0.81	2.54±0.32	15.3±0.55	8.23±0.29	
	6567	6.08±0.51	2.42±0.20	8.36±0.33	4.49±0.18	
	6568	6.80±0.85	2.71±0.34	7.32±0.47	3.93±0.25	
	7371	6.01±0.99	2.39±0.39	7.22±0.98	3.88±0.53	2.49±0.14

[1]Errors correspond to 1-σ statistical uncertainties.

[2]The average value for all observations per source for the Mg edge.